Fluid Phase Equilibria 290 (2010) 137–147

Contents lists available at ScienceDirect

Fluid Phase Equilibria

journal homepage: www.elsevier.com/locate/fluid

# Modeling the phase behavior, excess enthalpies and Henry's constants of the $H_2O + H_2S$ binary mixture using the SAFT-VR+D approach

M. Carolina dos Ramos [a], Clare McCabe [a,b,*]

[a] Department of Chemical and Biomolecular Engineering, Vanderbilt University, Nashville, TN 37235, United States
[b] Department of Chemistry, Vanderbilt University, Nashville, TN 37235, United States

ARTICLE INFO

*Article history:*
Received 1 July 2009
Received in revised form 9 September 2009
Accepted 14 September 2009
Available online 23 September 2009

*Keywords:*
Equation of state
SAFT-VR+D
Phase behavior
Excess enthalpy
Henry's constants
Solubility
Polar systems
Hydrogen sulphide
Water

ABSTRACT

The high-pressure phase diagram and other thermodynamic properties of the binary systems of water + hydrogen sulphide have been examined using the SAFT-VR+D equation of state [Zhao and McCabe, J. Chem. Phys. 125 (2006) 104504]. The SAFT-VR+D approach is based on a version of the statistical associating fluid theory that was developed to model dipolar fluids by explicitly accounting for dipolar interactions and their effect on the thermodynamics and structure of a fluid. In the SAFT-VR+D equation this is achieved through the use of the generalized mean spherical approximation (GSMA) to describe a monomer fluid of dipolar square-well segments. In the present work, we further develop the SAFT-VR+D equation to study mixtures of dipolar associating fluids of arbitrary size using the analytical solution of the Ornstein–Zernike equation due to Cummings and Blum [J. Chem. Phys. 84, 1833 (1986)]. The high-pressure phase diagram and other thermodynamic properties of the water + hydrogen sulphide binary mixture are then examined. Both components, hydrogen sulphide and water, are naturally modeled as associating spherical molecules with four off-centre sites to mimic hydrogen bonding and an embedded dipole moment ($\mu$) to describe their polarity. Using simple Lorentz–Berthelot combining rules, the theory is able to predict the phase behavior of the $H_2O + H_2S$ system from pure component parameters. Specifically, type *III* phase behavior according to the classification of Scott and van Konynenburg is observed, with a three-phase line at low temperatures that terminates at an upper critical end point and two separate critical lines, one at high temperatures that runs continuously from a gas–liquid critical line to a liquid–liquid critical line at high pressures and a second gas–liquid critical line located at low temperatures. The phase behavior predicted by the SAFT-VR+D approach is in excellent agreement with the experimental data, without requiring any fitted binary interaction parameters. In addition, the theory is also able to describe the excess molar enthalpies and the most important features of the Henry's constants as a function of temperature.



## 1. Introduction

Both water and hydrogen sulphide are encountered in several industrial operations, including pulp and paper processes [1,2] and natural gas and petroleum exploration and production [3]. Hydrogen sulphide in particular is formed during the de-sulphurization of crude oil streams [4], which if untreated can cause the deposition of heavy organic molecules such as asphaltenes and lead to corrosion in wells, pipelines and refining equipment [5]. Sulphur compounds are widely recognized as one of the most undesirable polluting agents. Hydrogen sulphide for example is harmful at elevated concentrations to living organisms [1,6], pollutes groundwater, and can form an explosive mixture with air [7]. As a result, there is a growing challenge to reduce the atmospheric emissions of hydrogen sulphide, and other acid gases, to meet environmental restrictions and regulations [8]. Therefore, an accurate knowledge of the phase behavior of mixtures involving hydrogen sulphide is important to plant design and operation within the chemical industry [5,8,9].

The system water + hydrogen sulphide has been studied extensively and a large amount of experimental data is available [7,9–24], which has been recently reviewed by Carroll et al. [20,21,25], Chapoy et al. [9], and Koschel et al. [7]. While most of the experimental data is focused on the mutual solubility of the water + hydrogen sulphide system [9–23,25], there is interest in hydrate formation conditions [9,10], as well as the effect of salt on the solubility of hydrogen sulphide in water [11,16,19,22]. Most of these experimental studies are limited to low temperature and pressure conditions because pure hydrogen sulphide decomposes at temperature above 444 K [26], which makes data at high temperatures both difficult and unsafe to collect. Additionally, the corrosive behavior of hydrogen sulphide solutions intensifies as temperature increases making the measurements more difficult

* Corresponding author. Tel.: +1 615 322 6853; fax: +1 615 343 7951.
*E-mail address:* c.mccabe@vanderbilt.edu (C. McCabe).

0378-3812/$ – see front matter © 2009 Elsevier B.V. All rights reserved.
doi:10.1016/j.fluid.2009.09.018

and resulting in less reliable data [27]. Given the experimental challenges of studying this system, it is desirable to have reliable information on the thermodynamics and phase behavior from a theoretical approach.

From a theoretical point of view, both water and hydrogen sulphide are very interesting molecules to study due to the influence of the permanent dipole moment on the thermodynamics and phase behavior. It is known that polar interactions can greatly affect the phase behavior of pure components and their mixtures and so a non-ideal phase behavior is expected for the water + $H_2S$ system. This is confirmed by the type *III* phase behavior observed, in the classification of Scott and van Konynenburg, and the characteristic large regions of liquid–liquid separation.

Over the last decade, an important advance in the prediction of the thermodynamic properties of fluids has been achieved through the application of statistical mechanics based approaches. Molecular-based equations of state, such as those derived from the statistical associating fluid theory (SAFT), provide a framework in which the different microscopic effects such as nonsphericity and association interactions can be estimated and quantified separately, often leading to predictive and reliable equations of state applicable to complex systems. The SAFT equation was originally proposed by Chapman et al. [28,29], based on Wertheim's thermodynamic perturbation theory [30–33], and has since been applied to describe a wide range of fluids and many variations on the original expressions have been introduced [34–36]. Typically, when the SAFT approach has been applied to study multipolar fluids, such as water [37–39,88], refrigerants [40], carbon dioxide and their mixtures [41–44,88,89], the dipolar and quadrupolar interactions are treated in an effective manner via the segment size and energy parameters that describe the van der Waals interactions and/or through association interaction parameters; however, more recently, an effort has been made to incorporate dipolar interactions into the SAFT EOS directly by adding a dipolar contribution to the Helmholtz free energy [45–54]. In these equations the dipolar term is commonly described using the $\mu$-expansion proposed by Gubbins and Gray [55] or the Padé approximation of Stell et al. [56], in which nonspherical dipolar molecules are approximated by spherical molecules and the orientation of the dipolar interaction is not accounted for. Since the SAFT equation is widely used to model chain fluids, Jog et al. [49,50] have proposed a Padé dipolar term that is applied at the segment, rather than molecule level, and has been used by Tumakaka and Sadowski [57] within the perturbed chain SAFT (PC-SAFT) equation to describe mixtures of polar and nonpolar fluids. PC-SAFT has also been extended to account for dipole–dipole, dipole–quadrupole, quadrupole–quadrupole and dipole-induced dipole interactions by Karakatsani and Economou [53,54] using perturbation theory proposed by Larsen et al. [58]. The new equation has been applied to study a wide range of polar fluids and their mixtures [53,55,59,60], and the inclusion of polar interactions found to improve the theoretical predictions in most cases [59]. Alternatively, expressions for incorporating dipolar interactions can be derived from molecular simulation, as in the work of Gross and coworkers [51,52] who have proposed dipolar and quadrupolar terms based on simulation data for the vapor–liquid equilibria of the two-center Lennard–Jones plus point dipole/quadrupole fluid.

Although in these approaches the dipolar interactions are applied at the segment level, the effect of the dipole on the structure of the fluid, and in turn the thermodynamic properties, is not explicitly considered since the chain term is not modified to account for the effect of the dipole when applying the theory to chain fluids. In contrast, in the SAFT-VR+D approach [61,62] we have obtained the anisotropic dipolar contribution to the free energy at both the segment and chain level from Wertheim's solution [63] of the Ornstein–Zernike (OZ) equation for dipolar hard spheres and chains with mixed dipole moments using the mean spherical approximation (MSA) and linearized exponential (LEXP) approximation closures. This allows us to model chain fluids in which one or more specific segments can be dipolar and to capture the effect of the dipolar interactions on both the structure and thermodynamics of the fluid explicitly. Before application to real fluids, the SAFT-VR+D equation was tested extensively against computer simulation data [61,62] for dipolar square-well monomer and chain fluids in which one or more segments are dipolar. Good agreement between the theoretical predictions and simulation data was obtained demonstrating that the SAFT-VR+D equation provides a good description of the phase behavior of both dipolar monomer and chain fluids. Subsequently, we applied the approach to mixtures of dipolar associating fluids with non-polar fluids such as $H_2S$ + *n*-alkane binary mixtures [65], based on the work of Adelman and Deutch [66], who provided an exact solution to the MSA for simple polar mixtures of equal diameters in terms of an effective single component fluid. In the present work, we further develop the SAFT-VR+D approach to study mixtures of dipolar associating fluids of arbitrary size, based on the analytical solution to the MSA due to Cummings and Blum [66,67] for mixtures of dipoles of unequal diameter, thereby explicitly accounting for the dipolar interactions of each polar compound. We then apply the theory to examine the global fluid phase behavior of the water + hydrogen sulphide binary mixture.

For both water [62] and hydrogen sulphide [64] we use the molecular parameters developed in previous work. The unlike interaction parameters between different compounds are then obtained using simple Lorentz–Berthelot combining rules and so only the pure component intermolecular parameters were fitted to experimental data. In this manner, the ability of the SAFT-VR+D approach to predict the thermodynamic properties of the water + $H_2S$ system can be tested. In addition, we also test the ability of the theory to predict the excess molar enthalpy and the infinite-dilution Henry's constants of the mixture by comparison with the corresponding experimental data. This is a very interesting test of the equation, since excess thermodynamic properties tend to be more sensitive to the details of the molecular model than the phase equilibria properties [68–70].

The remainder of the paper is organized as follows: the molecular model and theory are described in Section 2, the results and discussion are presented in Section 3, and conclusions discussed in Section 4.

## 2. Molecular model and theory

In this work, water is described by the widely used four-site SAFT water model that is based on the work of Bol [71] and Nezbeda et al. [72], with the addition of an embedded dipole moment. Therefore within the SAFT-VR+D approach the water molecules are represented by an associating dipolar hard-core segment of diameter $\sigma_{11}$, with an embedded dipole moment $\mu_{11}$, that also interacts via a square-well potential of depth $\varepsilon_{11}$ and range $\lambda_{11}$, and four off-centre short-range attractive sites to describe the self-association; two sites of type H represent the hydrogen atoms and two sites of type O represent the lone pairs of electrons on the oxygen atom with only H–O site–site interactions allowed. Similarly, hydrogen sulphide is modeled by a four-site model [64,73,74] as a dipolar hard-core segment of diameter $\sigma_{22}$, with an embedded dipole moment $\mu_{22}$, that interacts via a square-well potential of a depth $\varepsilon_{22}$ and range $\lambda_{22}$, and four off-centre short-range attractive sites to describe the self-association. Two sites of type H represent the hydrogen atoms and two sites of type S represent the lone pairs of electrons on the sulphur atom. Only H–S site–site interactions are allowed. The sites of both models are located at a distance $r_d^* = 0.25$ from the centre of the sphere and have a cut-off range of $r_c$ so that

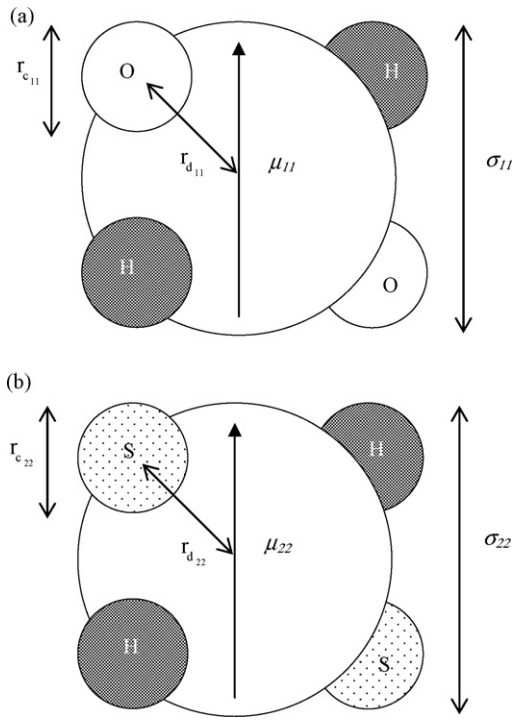


**Fig. 1.** Schematic representation of the models used to describe the (a) water and (b) hydrogen sulphide molecules. A spherical segment with a dipole moment $\mu$ is embedded in the centre of a monomer segment with four square-well bonding sites. Water has two sites of type H and two sites of type O placed at a distance $r_{d11}$ off-centre of a sphere of hard-core diameter $\sigma_{11}$. Only the H–O bonding interaction is allowed when the two sites are closer than a distance $r_{c11}$ apart. Similarly, $H_2S$ has two sites of type H and two sites of type S placed at a distance $r_{d22}$ off-centre of a sphere of hard-core diameter $\sigma_{22}$ and only the H–S bonding interaction is allowed when the two sites are closer than a distance $r_{c22}$ apart.

an attractive energy $\varepsilon^{HB}$ is realized if sites are closer than a distance $r_c$ apart. This geometry defines the volume available ($K_{ii}^{HB}$) for the site–site hydrogen bonding association. These models are schematically represented in Fig. 1 and have been previously used to describe the phase behavior of pure water [62], hydrogen sulphide, and mixtures of hydrogen sulphide with alkanes [64] by the authors within the SAFT-VR+D approach.

In the SAFT-VR+D approach, the inclusion of the dipole–dipole interactions are accounted for through the dipole moment $\mu$ and the orientation of the dipoles which is determined by the azimuthal $\theta$ and polar $\phi$ angles of the inter-segment axis along $r$, as shown in Fig. 2 [75]. Therefore, the pair potential for a mixture of dipolar associating molecules is defined as,

$$u_{ij}(\mathbf{r}_{ij}\mathbf{w}_1\mathbf{w}_2) = u_{ij}^{HS}(r_{ij};\sigma_{ij}) - \varepsilon_{ij}\phi_{ij}^{SW}(r_{ij};\lambda_{ij}) + u_{ij}^{dipole}(\mathbf{r}_{ij}\mathbf{w}_1\mathbf{w}_2) + \sum_{A_i}\sum_{B_j} u_{A_iB_j}^{HB}(\mathbf{r}_{ij}\Omega_1\Omega_2) \quad (1)$$

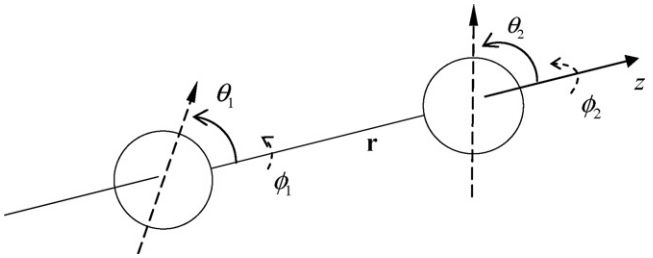


**Fig. 2.** Schematic representation of the interdipole site coordinate system with polar axis along $r$ [75].

where $\mathbf{r}_{ij}$ is the vector between the center of species $i$ and $j$, $r_{ij} = |\mathbf{r}_{ij}|$ the distance between segments of species $i$ and $j$; $\mathbf{w}_i = (\theta_i, \phi_i)$ the set of angles that define the orientation of the dipole moment in the monomer of species $i$; and $\Omega_i$ the orientation of the association site $i$ relative to the vector $\mathbf{r}_{ij}$. The isotropic terms in Eq. (1), as in the SAFT-VR equation [76,77], consist of a hard-sphere repulsive interaction $u_{ij}^{HS}(r_{ij};\sigma_{ij})$ defined by,

$$u_{ij}^{HS}\left(r_{ij};\sigma_{ij}\right) = \begin{cases} \infty & \text{if} \quad r_{ij} \le \sigma_{ij} \\ 0 & \text{if} \quad r_{ij} > \sigma_{ij} \end{cases} \quad (2)$$

and an attractive term $-\varepsilon_{ij}\phi_{ij}^{SW}(r_{ij};\lambda_{ij})$ modeled by a square-well potential of depth $\varepsilon_{ij}$ and shape $\phi_{ij}^{SW}(r_{ij};\lambda_{ij})$ defined by,

$$\phi_{ij}^{SW}\left(r_{ij};\lambda_{ij}\right) = \begin{cases} 1 & \text{if} \quad \sigma_{ij} < r_{ij} \le \lambda_{ij}\sigma_{ij} \\ 0 & \text{if} \quad r_{ij} > \lambda_{ij}\sigma_{ij} \end{cases} \quad (3)$$

where $\lambda_{ij}$ is the parameter associated with the range of the square-well potential. The anisotropic dipole–dipole potential $u_{ij}^{dipole}(\mathbf{r}_{ij}\mathbf{w}_1\mathbf{w}_2)$ is a long-range anisotropic interaction, which can be expressed as,

$$u_{ij}^{dipole}(\mathbf{r}_{ij}\mathbf{w}_1\mathbf{w}_2) = -\frac{\mu_i\mu_j}{r_{ij}^3} D_{ij}(\mathbf{n_1}\mathbf{n_2}\hat{\mathbf{r}}_{\mathbf{ij}}) \quad (4)$$

where

$$D_{ij}(\mathbf{n_1}\mathbf{n_2}\hat{\mathbf{r}}_{\mathbf{ij}}) = [3\mathbf{n_1}\cdot\hat{\mathbf{r}}_{\mathbf{ij}}\mathbf{n_2}\cdot\hat{\mathbf{r}}_{\mathbf{ij}} - \mathbf{n_1}\cdot\mathbf{n_2}] \quad (5)$$

Here $\hat{\mathbf{r}}_{\mathbf{ij}}$ is the unit vector in the direction of $\mathbf{r}_{ij}$ and $\mathbf{n}_i$ is a unit vector parallel to the dipole moment on segment $i$. Finally, the association potential $u_{A_iB_i}^{HB}$ models site–site association interactions between molecules through an anisotropic short-range square-well interaction, where $A_i$ and $B_j$ are interacting associating sites on species $i$ and $j$, respectively.

Within the SAFT framework, the Helmholtz free energy $A$ of a mixture of dipolar associating spherical segments can be written in the form,

$$\frac{A}{Nk_BT} = \frac{A^{IDEAL}}{Nk_BT} + \frac{A^{MONO}}{Nk_BT} + \frac{A^{ASSOC}}{Nk_BT} \quad (6)$$

where $N$ is the total number of molecules, $T$ is the temperature, $k_B$ the Boltzmann constant, $A^{IDEAL}$ the free energy of the ideal fluid, $A^{MONO}$ the contribution due to the dipolar square-well monomer reference fluid and $A^{ASSOC}$ the free energy contribution due to intermolecular association. We now describe each of the terms in Eq. (6) in turn below.

### 2.1. Ideal contribution

The free energy of an ideal mixture of $n$ components is given by [78],

$$\frac{A^{IDEAL}}{Nk_BT} = \sum_{i=1}^{n} x_i \ln\left(\rho_i\Lambda_i^3\right) - 1 \quad (7)$$

where $\rho_i = N_i/V$ is the number density, $x_i$ the molar fraction and $\Lambda_i$ the thermal de Broglie wavelength of species $i$.

### 2.2. Monomer contribution

The contribution to the Helmholtz free energy due to the monomer segments is given by,

$$\frac{A^{MONO}}{Nk_BT} = \left(\sum_{i=1}^{n} x_i m_i\right)\frac{A^{M}}{N_s k_B T} = \left(\sum_{i=1}^{n} x_i m_i\right) a^{M} \quad (8)$$

where $N_s$ is the total number of spherical monomers. Within the generalized mean spherical approximation (GMSA) the excess Helmholtz free energy per monomer $a^M$ is given by the free energy per monomer of the dipolar square-well reference fluid $a^{DSW}$, which in turn can be written as,

$$a^M = a^{DSW} = a^{dipole} + a^{isotropic} \tag{9}$$

Here $a^{dipole}$ describes the contribution to the free energy due to the anisotropic dipolar interactions and $a^{isotropic}$ is written in terms of the inverse of the temperature $\beta = 1/k_BT$ within a second-order high-temperature perturbation expansion due to Barker and Henderson [79–81],

$$a^{isotropic} = a^{HS} + \beta a_1 + \beta^2 a_2 \tag{10}$$

where $a^{HS}$ is the free energy due to repulsive interactions between the hard cores, and $a_1$ and $a_2$ are the first and second-order perturbative terms associated with the isotropic attractive interactions, respectively. The residual free energy of the hard-sphere mixture is obtained from the expression of Boublik [82] and Mansoori et al. [83]. The mean-attractive energy associated with the first-order perturbation term is treated in the context of the M1Xb mixing rules [77] and the second-order perturbation term is obtained using the local compressibility approximation as in the original SAFT-VR approach [76].

The anisotropic dipolar contribution comes from the solution of the Ornstein–Zernike equation for dipolar hard spheres of arbitrary size using the MSA closure. In the work of Cummings and Blum [66,67], the solution is given in terms of the excess internal energy, expressed by

$$u_{int}^{dipole} = -3\sum_{i=1}^{n}\sum_{j=1}^{n}\sqrt{x_i x_j}\, y_{ij} k_{ij} \tag{11}$$

where $y_{ij}$, the so-called strength of the dipolar effects [63], is given by,

$$y_{ij} = \frac{4\pi\beta\rho_i^{1/2}\mu_i\rho_j^{1/2}\mu_j}{9} \tag{12}$$

and $k_{ij}$ correspond to the scaling parameters, which are obtained from the solution of the OZ equation for dipolar hard spheres of arbitrary size in the MSA. These parameters are defined in terms of the expansion coefficient ($\hat{h}_{ij}^{112}(r)$) of the total correlation function and expressed as,

$$k_{ij} = \sqrt{\frac{3}{10}}\int_0^\infty \frac{\hat{h}_{ij}^{112}(r)}{r}\mathrm{d}r \tag{13}$$

The Helmholtz free energy of a dipolar mixture can be obtained from the Gibbs–Helmholtz energy equation by an inverse temperature integration of the excess internal energy, written as,

$$a^{dipole} = -\frac{3}{\beta}\sum_{i=1}^{n}\sum_{j=1}^{n}\sqrt{x_i x_j}\, y_{ij}\int_0^\beta k_{ij}(\beta')d\beta' \tag{14}$$

where $\beta = 1/k_BT$, $\beta' = 1/k_BT'$ with $\beta = 0$ corresponding to the hard-sphere case. $k_{ij}(\beta')$ indicates the explicit inverse temperature dependence of the scaling parameters. As pointed out by Isbister et al. [84], the integral on the right-hand side of Eq. (13) must be solved numerically since the integration by parts technique used in the pure case cannot be used in the present case. Following their work, we have also used an 8-point Gaussian quadrature to solve the integral.

The scaling parameters are then determined from the $y_{ij}$ values, which are known at a given temperature, density and dipole moment, by considering the closure of the direct correlation function (in terms of the expansion coefficient $\hat{c}_{ij}^{112}(r)$). The solution is expressed by the $n(n+1)/2$ equations written in a matrix form,

$$3[y] = [q_1] - [q_2] \tag{15}$$

where the square brackets denote an $n \times n$ matrix quantity, the $y_{ij}$ values are the elements of the $[y]$ matrix, and $\mathbf{I}$ is the identity matrix. Following the notation of Cumings and Blum, the matrices $[q_1]$ and $[q_2]$ are defined by

$$[q_1] = \{\mathbf{I} - [\rho^{1/2}][K_0^0][\rho^{1/2}]\}\{\mathbf{I} - [\rho^{1/2}][K_0^0][\rho^{1/2}]\}^T \tag{16}$$

$$[q_2] = \{\mathbf{I} - [\rho^{1/2}][K_1^0][\rho^{1/2}]\}\{\mathbf{I} - [\rho^{1/2}][K_1^0][\rho^{1/2}]\}^T \tag{17}$$

where $T$ indicates the respective matrix transpose, and the matrices $[\rho^{1/2}]$, $[\sigma]$, $[K_0^0]$ and $[K_1^0]$ are given by the following expressions,

$$[\rho^{1/2}]_{ij} = \delta_{ij}\rho_i^{1/2} \tag{18}$$

$$[\sigma]_{ij} = \delta_{ij}\sigma_i \tag{19}$$

$$[K_0^0]_{ij} = -\frac{1}{2}\sigma_i^2[b_0]_{ij} - \frac{1}{12}\sigma_i^3[a_0]_{ij} \tag{20}$$

$$[K_1^0]_{ij} = -\frac{1}{2}\sigma_i^2[b_1]_{ij} - \frac{1}{12}\sigma_i^3[a_1]_{ij} \tag{21}$$

where the $\delta_{ij}$ is the delta function, the elements of $[K_0^0]$ and $[K_1^0]$ are expressed directly in terms of $[a_0]$, $[b_0]$, $[a_1]$, and $[b_1]$, which are given in turn in terms of the elements of $[k]$, expressed as,

$$[a_0] = 4\pi[k]\{\mathbf{I} - 2[z_3][k]\}^{-1}\{\mathbf{I} - 2[z_2][k][\sigma]\}^{-1}\{\mathbf{I} + 4[z_2][k][\sigma]\} \tag{22}$$

$$\mathbf{I} + \frac{1}{\pi}[z_2][b_0] = \{\mathbf{I} - 2[z_2][k][\sigma]\}^{-1} \tag{23}$$

$$[a_1] = -2\pi[k]\{\mathbf{I} + [z_3][k]^{-1}\}\{\mathbf{I} + [z_2][k][\sigma]\}^{-1}\{\mathbf{I} - 2[z_2][k][\sigma]\} \tag{24}$$

$$\mathbf{I} + \frac{1}{\pi}[z_2][b_1] = \{\mathbf{I} + [z_2][k][\sigma]\}^{-1} \tag{25}$$

where we have defined the matrices $[z_2]$ and $[z_3]$ by,

$$[z_t]_{ij} = \delta_{ij}\frac{\pi}{6}\rho_i\sigma_i^t \tag{26}$$

In summary, the solution of the OZ equation reduces to finding the values of the $k_{ij}$ elements of the matrix $[k]$ that satisfy the $n(n+1)/2$ equations presented in Eq. (14) given the values of $[y]$. Once the $[k]$ values have been determined, the contributions to the internal and Helmholtz free energies can be easily obtained from Eqs. (11) and (13). For further details on the general solutions of the OZ equations with the MSA closure we direct the reader to the work of Cummings and Blum [66,67].

### 2.3. Association contribution

The contribution to the free energy due to the association of $s_i$ sites on a molecule of species $i$ can be obtained from Wertheim's theory as,

$$\frac{A^{ASSOC}}{Nk_BT} = \sum_{i=1}^{n} x_i\left[\sum_{a=1}^{s_i}\left(\ln X_{a,i} - \frac{X_{a,i}}{2}\right) + \frac{s_i}{2}\right] \tag{27}$$

where the first sum is over species $i$ and the second sum is over all $s_i$ sites of type $a$ on a molecule $i$, and $X_{a,i}$ is the fraction of molecules $i$ not bonded at site $a$, given by the mass action equation as [26,27],

$$X_{a,i} = \frac{1}{1 + \rho\sum_{j=1}^{n} x_j\sum_{b=1}^{s_j} X_{b,j}\Delta_{a,b,i,j}} \tag{28}$$

Here $\Delta_{a,b,i,j}$ characterizes the association between site $a$ on molecule $i$ and site $b$ on molecule $j$ and can be written as:

$$\Delta_{a,b,i,j} = K_{a,b,i,j} f_{a,b,i,j} g_{ij}^{SW}(\sigma_{ij}) \tag{29}$$

where $g_{ij}^{SW}(\sigma_{ij})$ is the contact value of the radial distribution function, $f_{a,b,i,j} = \exp(-\phi_{a,b,i,j}/k_B T) - 1$ the Mayer $f$-function for the $a$–$b$ site-site interaction $\phi_{a,b,i,j}$, and $K_{a,b,i,j}$ the volume available for bonding.

The study of phase equilibrium in mixtures also requires the determination of a number of cross interaction parameters, which account for the interactions between unlike components in the mixture. The Lorentz arithmetic mean is used for the unlike hard-core diameter,

$$\sigma_{12} = \frac{\sigma_{11} + \sigma_{22}}{2} \tag{30}$$

the unlike square-well dispersive energy is given by the Berthelot rule,

$$\varepsilon_{12} = \sqrt{\varepsilon_{11}\varepsilon_{22}} \tag{31}$$

and the unlike square-well potential range is determined by,

$$\lambda_{12} = \frac{\lambda_{11}\sigma_{11} + \lambda_{22}\sigma_{22}}{\sigma_{11} + \sigma_{22}} \tag{32}$$

For the unlike association interactions, only certain interactions between sites on the water and hydrogen sulphide models are permitted. In particular, the unlike association between sites of type H in the water molecule and sites of type S in the hydrogen sulphide and between sites type O in the water molecule and sites type H in the hydrogen sulphide are allowed. No S–O or H–H unlike association interactions are permitted. The site–site unlike association energy is given by the Berthelot rule as follows,

$$\varepsilon_{12}^{HB} = \sqrt{\varepsilon_{11}^{HB}\varepsilon_{22}^{HB}} \tag{33}$$

and the bonding volume available for association between sites on different molecules is determined by,

$$K^{HB} = \left[\frac{(K_{11}^{HB})^{1/3} + (K_{22}^{HB})^{1/3}}{2}\right]^3 \tag{34}$$

With the expression for the Helmholtz free energy defined thermodynamic properties such as the chemical potential, compressibility factor, and other thermodynamic derivatives, can be easily obtained using standard thermodynamic relations.

## 3. Results and discussion

In this section we present the theoretical predictions obtained using the SAFT-VR+D equation to describe the phase behavior, excess enthalpies, and Henry's constants of the water + hydrogen sulphide binary mixture. The intermolecular model parameters used for water and hydrogen sulphide have been presented previously [62,64], and have been shown to provide an excellent description of the pure vapor–liquid equilibria. Both components are modeled as a square-well spherical segment with an embedded dipole moment and four associating sites, as described in the previous section; in each case the experimental dipole moment was used with the remaining parameters fitted to experimental vapor pressure and saturated liquid density data. The optimized values for the hard-core diameter ($\sigma_{ii}$), square-well potential depth ($\varepsilon_{ii}$) and range ($\lambda_{ii}$) and the self-association parameters ($\varepsilon^{HB}$ and $K^{HB}$) are presented in Table 1. Since we use the Lorentz–Berthelot (LB) combining rules for the unlike interactions, the results presented here for the water + hydrogen sulphide binary mixture are pure predictions. It is important to mention that when using the set of optimized parameters shown in Table 1, the theory will over predict the pure component critical points, due to the fact that, as with most engineering equations of state, the SAFT-VR+D equation does not include the long-range density fluctuations that occur near the critical point of real fluids [85,88,89]. This can be overcome through the incorporation of so-called crossover techniques (see for example [88–91] and the references therein) into the equation of state or by re-scaling the pure component parameters to the experimental values of the critical point. Using this procedure, the values of the rescaled parameters for hydrogen sulphide and water are also presented in Table 1. While, we have used the optimized parameters for all the calculations in the present work, in the case of the *PT* projection, we have also included the results obtained using the rescaled parameters for a complete comparison.

**Table 1**
Optimized and rescaled (indicated by the asterisk) intermolecular parameters for hydrogen sulphide and water used in SAFT-VR+D approach.

| | $H_2O$[a] | $H_2S$[b] |
|---|---|---|
| $\mu$ (D) | 1.84 | 0.97 |
| $m$ | 1 | 1 |
| $\sigma$ (Å) | 3.061 | 3.67295 |
| $\varepsilon/k_B$ (K) | 389.87 | 212.4090 |
| $\lambda$ | 1.48 | 1.6255 |
| $\varepsilon^{HB}/k_B$ (K) | 900.55 | 501.69791 |
| $K^{HB}$ (Å$^3$) | 1.467 | 1.5000 |
| $\sigma^*$ (Å) | 3.6216 | 3.88160 |
| $\varepsilon^*/k_B$ (K) | 381.9922 | 204.8186 |
| $\varepsilon^{HB*}/k_B$ (K) | 882.3532 | 482.8249 |
| $K^{HB*}$ (Å$^3$) | 2.429633 | 1.76099 |

[a] Optimized parameters taken from reference [62].
[b] Optimized parameters taken from reference [64].

### 3.1. Phase behavior

We first consider the high-pressure phase behavior of the binary mixture of $H_2O + H_2S$. Fig. 3 shows the SAFT-VR+D theoretical predictions of the *PT* projection of the *PTx* surface for the mixture using both the optimized and the rescaled parameters. As can be seen from the figure, the main feature of the diagram is a large region of liquid–liquid (LL) immiscibility that dominates the phase behavior; the mixture exhibits type *III* phase behavior according to the Scott and van Konynenburg classification scheme [86,87]. In Fig. 3a, following the results obtained from the optimized parameters, we see that the high-temperature critical line starts at the liquid–vapor critical point of the less volatile component (water) and moves towards lower temperatures exhibiting an almost flat region initially that contains a very small pressure maximum (at 36.9 MPa and approximately 660 K) followed by a very small pressure minimum (at 36.66 MPa at approximately 640 K). Following the pressure minimum, the critical line runs to higher pressures with a negative slope until it reaches a temperature minimum (at approximately 409 K) at very high pressures (~1800 MPa), which continues to higher pressures and temperatures with a very steep but positive slope, as can be seen in Fig. 3b. Note that this temperature minimum cannot be observed in Fig. 3a due to the pressure scale. The second, shorter, critical line, which connects the vapor–liquid critical point of pure hydrogen sulphide and the upper critical end point (UCEP with $T_{UCEP}$ = 405.7 K and $P_{UCEP} \approx 12.3$ MPa), is located at low temperatures and pressures (see inset Fig. 3b). The presence of the UCEP point marks the start of the three-phase liquid–liquid–vapor region, where the two immiscible liquid phases coexist with a vapor phase and extends to low temperatures and pressures. The presence of the temperature minimum in the high-temperature critical line could also indicate the presence of *gas–gas immiscibility of the second kind*; however, the term gas–gas immiscibility is usually used to describe the presence of a two fluid phase region that coexists in equilibrium at temperatures higher than both pure critical points. Since the slope of the curve after the temperature minimum is very steep, the gas–gas immiscibility would appear at extremely high pressures and so

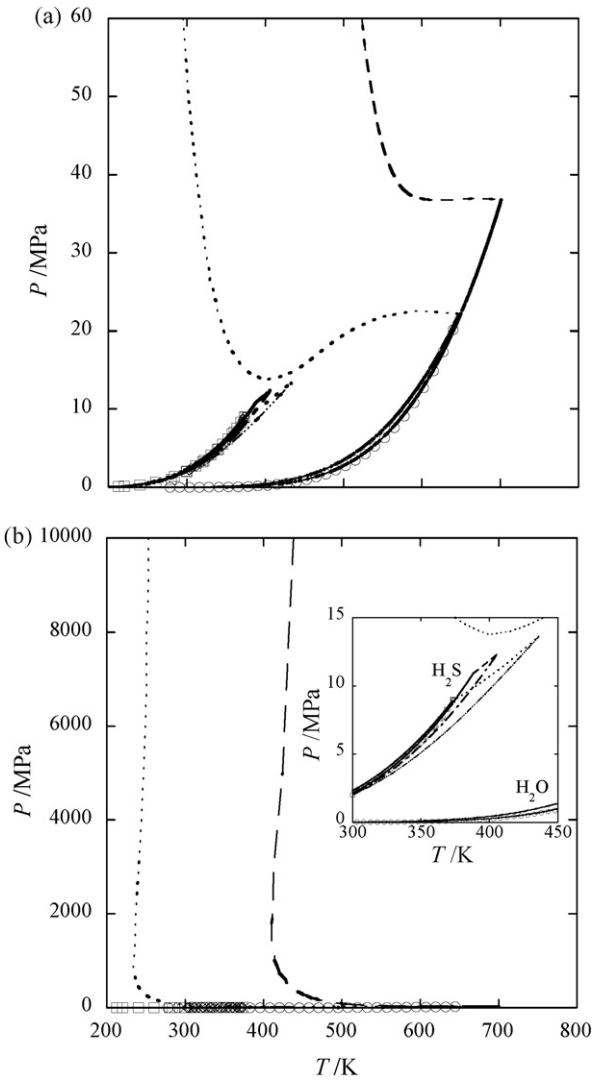


**Fig. 3.** *PT* projection of the *PTx* surface for the $H_2O$ (1) + $H_2S$ (2) binary mixture. Circles, squares and diamonds correspond to experimental data for the vapor pressure curves of pure water [93] and pure hydrogen sulphide [94–96], and the three-phase liquid–liquid–vapor line (LLV) [10], respectively. Solid, dashed and dot-dashed lines correspond respectively to the pure component vapor pressures, critical lines and three-phase liquid–liquid–vapor coexistence predictions from the SAFT-VR+D approach using the optimized parameters. Thin-solid lines, dotted lines and dot-dashed lines correspond to the pure component vapor pressures, critical lines and three-phase liquid–liquid–vapor line predictions from the SAFT-VR+D approach using rescaled intermolecular parameters. Part (a) shows the *PT* projection over the range of experimental interest while part (b) shows a larger pressure scale in order to observe the temperature minimum in the high-pressure critical line in the *PT* representation. The inset in part (b) highlights the region of liquid–liquid immiscibility close to the critical point of pure $H_2S$.

solid phases may encounter the critical line before the critical temperature of water is reached. For comparison purposes, we have also included in the *PT* projection of Fig. 3 the results from the theory using the parameters rescaled to the critical point of water and hydrogen sulphide. As can be seen in Fig. 3, the theoretical predictions of the high-temperature critical line from the SAFT-VR+D approach using the rescaled parameters shows the same trend, i.e., the system still exhibits a type *III* diagram [86,87]; however, the critical line has shifted towards lower temperatures and pressures. The pressure minimum is now located at 400 K and ~13.80 MPa (see Fig. 3a), which is closer to the UCEP point ($T_{UCEP}$ = 436.1 K and $P_{UCEP} \approx$ 13.6 MPa) as seen in the inset of Fig. 3b, while the temperature minimum is located at approximately 253 K and 900 MPa (see Fig. 3b). This behavior is to be expected since the optimized parameters are known to overestimate the pure fluid critical points, while the rescaled parameters are in good agreement with the experimental critical temperature and pressure (though at the cost of agreement with experimental data in regions far from the critical point).

Fig. 4 shows a *Tx* diagram of the liquid–liquid–vapor coexistence at low temperature, which has been divided into hydrogen sulphide-rich and water-rich regions for clarity. As can be seen from the figure, the theory provides a good description of the experimentally phase observed behavior: the vapor phase and the hydrogen sulphide-rich liquid phase (see Fig. 4a) increases in composition as the temperature increases, until they merge at the UCEP point; while the water-rich liquid phase (see Fig. 4b) decreases in composition as the temperature is increased. The vapor phase compositions are in good agreement with the experimental data at low temperatures, except in regions near the critical point of the less volatile component due to an overestimation of the hydrogen sulphide critical point; however, both hydrogen sulphide-rich and water-rich liquid phase compositions show overestimations, which is particularly more marked on the hydrogen sulphide-rich liquid phase. This could be due to the unlike interactions between hydrogen sulphide and water not being strong enough relative to the hydrogen sulphide–hydrogen sulphide and water–water interactions, resulting in each liquid phase have a higher composition in the respective component.

In order to understand the different phase equilibria regions (LLE and VLE) in the water + hydrogen sulphide binary mixture we have predicted the phase behavior for different constant-temperature *Px*-slices of the *PTx* surface for which experimental data is available for comparison as shown in Figs. 5–7. In Fig. 5, two *Px*-slices at temperatures below both pure critical points are presented. At these conditions three homogeneous phases, a vapor, a water-rich liquid ($L_1$) and a hydrogen sulphide-rich liquid ($L_2$), bind the three two-phase coexistence envelopes ($L_1$–V, $L_2$–V, $L_1$–$L_2$) in each temperature slice. At pressures below the three-phase coexistence line, we observe the $L_1$–V region, which corresponds to the $H_2O$-rich liquid phase coexisting with the vapor phase, while at pressures above the $L_1$–$L_2$–V line, two regions can be observed: a large region of liquid–liquid immiscibility ($L_1$–$L_2$) and a small liquid–vapor ($L_2$–V) equilibria region, where the hydrogen sulphide-rich liquid phase coexists with the vapor phase. The experimental data correspond to the solubility of water in the hydrogen sulphide-rich phase (Fig. 5a) and the solubility of hydrogen sulphide in the water-rich phase (Fig. 5b) at low temperatures and pressures. Although the theory slightly underestimates the solubility of hydrogen sulphide in the water-rich phase, predicting higher water molar fractions, agreement between the experimental data and theoretical predictions is excellent for the solubility of water in the hydrogen sulphide-rich vapor phase. As we increase the temperature above both the critical point of the more volatile component and the UCEP point, the phase equilibria shifts towards higher pressures, the small $L_2$–V equilibria region disappears and no $L_1$–$L_2$–V three-phase equilibria exists, as seen in Fig. 6. At these conditions the system exhibits a fluid–fluid coexistence, which at low pressures has a $L_1$–V character that changes continuously to a $L_1$–$L_2$ character as the pressure is increased. In Fig. 6a, the solubility curve of water in the hydrogen sulphide-rich phase shows a minimum in pressure that is a remnant of the disappearing $L_2$–V equilibria region, which smoothly disappears as the temperature is increased, while in Fig. 6b, a change in the slope of the solubility of hydrogen sulphide in the water-rich phase appears due to the change from $L_1$–V to $L_1$–$L_2$ behavior. The agreement between the experimental data of Lee and Mather [15] and the theoretical predictions is very good, while a deviation is observed with the experimental data of Selleck et al. [10] (at 410.93 K and 444.26 K). From the experimental data in Fig. 4 we

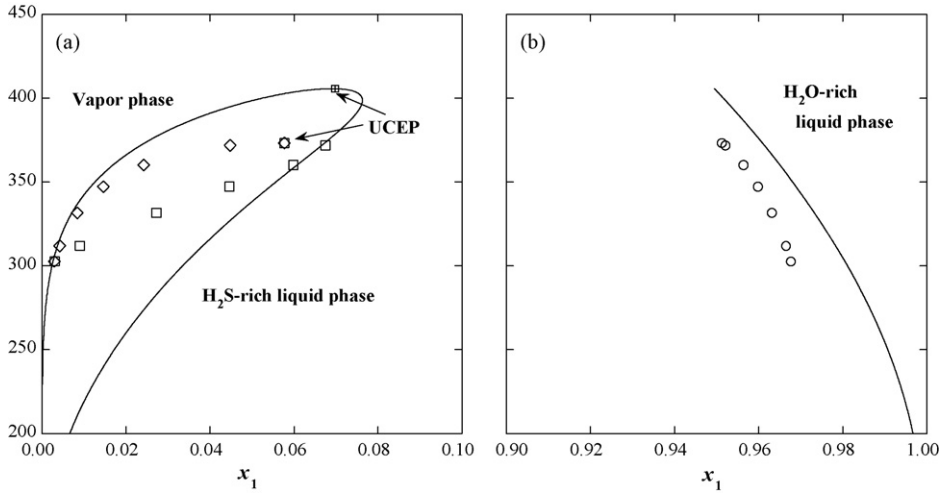


**Fig. 4.** *Tx* projection of the three-phase LLV line for the $H_2O$ (1) + $H_2S$ (2) binary mixture. Open symbols correspond to the experimental data [10], solid lines and the solid symbols represent the theoretical predictions of the LLVE and the UCEP using the SAFT-VR+D approach, respectively. Part (a) shows the results for the $H_2S$-rich liquid phase (□) and vapor phase (◊), and part (b) shows results for the water-rich liquid phase (○).

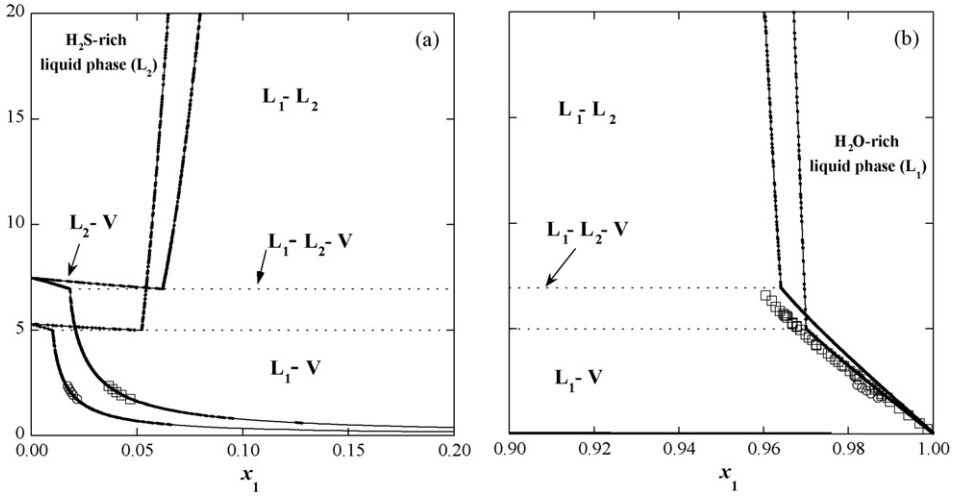


**Fig. 5.** *Px* projection of the *PTx* surface for the $H_2O$ (1) + $H_2S$ (2) binary mixture at temperatures below the critical point of pure $H_2S$. Part (a) shows the phase behavior at low water mole fractions and part (b) at mole fractions near pure water. Symbols correspond to the experimental data and lines represent the theoretical predictions of the two-phase coexistence (solid line) ($L_1$–$L_2$, $L_1$–V, $L_2$–V) and the three-phase $L_1$–$L_2$–V (dotted line) using the SAFT-VR+D approach at 343.15 K [12] (○), and 363.15 K [12,15] (□).

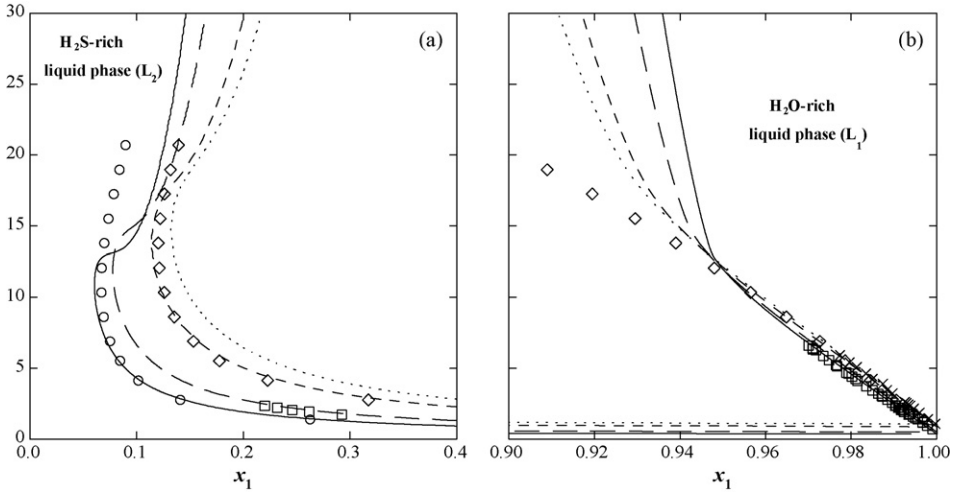


**Fig. 6.** *Px* projection of the *PTx* surface for the $H_2O$ (1) + $H_2S$ (2) binary mixture at intermediate temperatures above the UCEP temperature. Part (a) shows the phase behavior at low water mole fractions and part (b) at mole fractions close to pure water. Symbols correspond to the experimental data and lines represent the theoretical predictions of the LVE and LLE using the SAFT-VR+D approach at 410.93 K [10] (○ and solid line), 423.15 K [15] (□ and long-dashed line), 444.26 K [10] (◊ and dashed line), and 453.15 K (× and dotted line) [15].

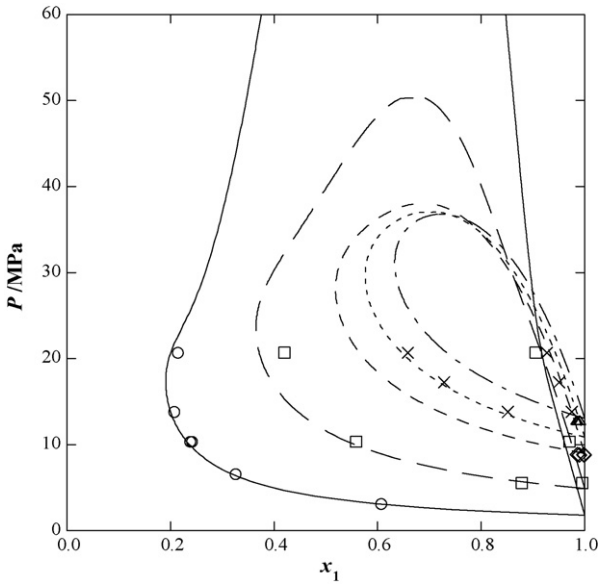


**Fig. 7.** *Px* projection of the *PTx* surface for the $H_2O$ (1) + $H_2S$ (2) binary mixture at high temperatures. Symbols correspond to the experimental data and lines represent the theoretical predictions of the LVE and LLE using the SAFT-VR+D approach at 477.59 K [17,18] (○ and solid line), 533.15 K [18] (□ and long-dashed line), 574.15 K [11] (◊ and dashed line), 588.15 K [18] (× and dotted line) and 603.15 K [11] (△ and dash-dotted line).

note that there appears to be some inconsistency in that the Selleck data does not follow the general trend of displaying a sharp change in curvature as pressure increases due to the disappearance of the $L_2$–V equilibria region. It has been previously noted [7,21,25] that discrepancies exist between different sets of experimental data for the $H_2O + H_2S$ system; in particular, in the work of Carroll and Mather [21] and Caroll [25] it was noted that despite the importance of the early work of Selleck et al. [10] in characterizing the phase equilibria of the $H_2O + H_2S$ system, care must be taken with their published smoothed data, since it was based on a few scattered data points and in some cases, the data points for the composition of the aqueous liquid phase at high pressures (above 13.79 MPa) was obtained by extrapolation of the solubility data at low pressure, which does not include the change of character from $L_1$–V to $L_1$–$L_2$. Considering this information and omitting the high-pressure experimental points at these temperatures, we can see that the agreement between the experimental data and theoretical predictions obtained from the SAFT-VR+D approach is very good.

As we increase the temperature further, the two-phase liquid–liquid region is reduced in size as shown in Fig. 7. Here the *Px*-slices are obtained at temperature values between the temperature minimum of the high-pressure critical line and the critical temperature of water, where the system exhibits a $L_1$–V coexistence region that extends from the vapor pressure curve of pure water up to the vapor–liquid critical point of the mixture at the corresponding temperature. Although not shown due to the scale of the graph, the two-phase equilibria at the lowest temperature presented (477.59 K) also exhibits a critical point (around 140 MPa). Overall, the SAFT-VR+D approach is able to provide an excellent description of the phase behavior of the $H_2O + H_2S$ system.

### 3.2. Excess molar enthalpies

Having successfully described the phase equilibria, we then examined the excess molar enthalpies of the water + hydrogen sulphide mixture. Since excess functions are usually more sensitive to molecular details than other properties, they can provide additional insight into the suitability of the model to accurately describe the thermodynamic behavior of the system of interest [68,92]. The excess molar enthalpy of the mixture ($H^E$) can be easily calculated from the molar enthalpies of the pure fluids ($H_i$) and the molar enthalpies of the mixture ($H_m$) at the same thermodynamic conditions of pressure and temperature using the standard thermodynamic relationship,

$$H^E = H_m - \sum_{i=1}^{n} x_i H_i \tag{35}$$

where the sum is over all components of the mixture. Note that the ideal enthalpy of mixing is zero so that the excess property is also equal to the enthalpy of mixing. Fig. 8 shows the excess molar enthalpy as a function of pressure at two different temperatures. The excess enthalpy is positive (enthalpy of mixing is endothermic) over the entire composition range and increases in magnitude as the pressure is increased. The excess enthalpy seems to exhibit a peculiar shape due to the presence of the large liquid–liquid immiscibility in the phase equilibria, dividing the excess enthalpy diagram into three different regions. The first and second regions correspond to the areas located at composi-

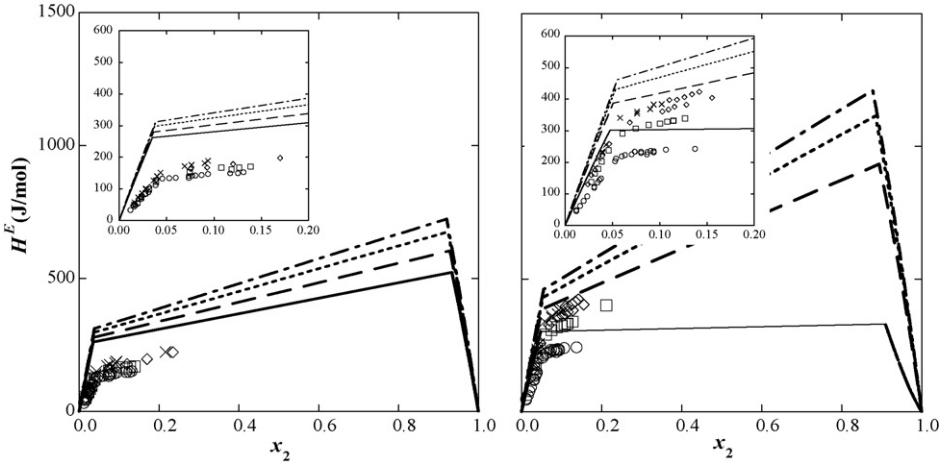


**Fig. 8.** Excess molar enthalpy of the $H_2O$ (1) + $H_2S$ (2) binary mixture at different thermodynamic conditions. Lines represent theoretical predictions from the SAFT-VR+D approach. Symbols correspond to experimental data of Koschel et al. [7]. In part (a) the system is at 353.1 K and pressures of 14.02 MPa (○ and solid line), 19.06 MPa (□ and long-dash line), 25.45 MPa (◊ and dotted line) and 30.86 MPa (× and dash-dot line). In part (b) the system is at 393.1 K and pressures of 13.58 MPa (○ and solid line), 19.86 MPa (□ and log-dash edline), 25.48 MPa (◊ and dotted line) and 30.28 MPa (× and dash-dotted line). The insets show the compositions near pure water.

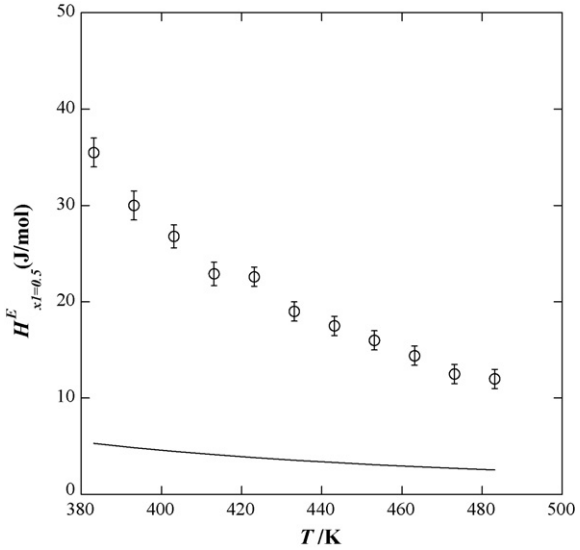


**Fig. 9.** Excess molar enthalpy at 0.101325 MPa of an equimolar binary mixture of $H_2O$ (1) + $H_2S$ (2) as a function of temperature. Solid lines represent the theoretical predictions from SAFT-VR+D approach. Symbols correspond to experimental data from Wormald [24] (○).

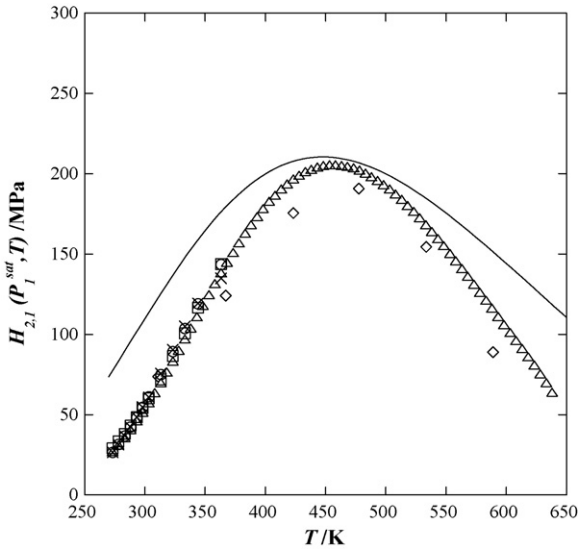


**Fig. 10.** Henry's coefficients under saturation vapor pressure as a function of temperature for the $H_2O$ (1) + $H_2S$ (2) binary mixture. Solid lines represent the theoretical predictions from SAFT-VR+D approach. Symbols correspond to experimental data from Clarke and Glew [13] (○), Lee and Mather [15] (□), Guillespie and Wilson [18] (◊), Caroll [21] (×) and Suleimenov [22] (△).

tions near pure water and pure hydrogen sulphide, respectively, where the system exhibits a homogeneous liquid phase. The third region corresponds to the intermediate compositions, where the system exhibits a two-phase fluid–fluid separation. Here, the $H^E$ is a straight line that connects the coexistence compositions at the temperature and pressure of the system. For example, the binary system $H_2O + H_2S$ at $T = 353.1$ K and $P = 14.02$ MPa exhibits phase separation at coexistence compositions of $x_2 = 0.03481$ and $x_2 = 0.93330$. In this case, the three regions are easily identified as: the $H_2O$-rich one-phase region that goes from $x_2 = 0.0$ to $x_2 = 0.03481$, the hydrogen sulphide-rich one-phase region that runs from $x_2 = 0.93330$ to $x_2 = 1.0$, and the LL immiscibility region that is limited by $x_2 = 0.03481$ and $x_2 = 0.93330$. In the insets of Fig. 8 we show the values of $H^E$ at compositions near pure water where experimental data is available. As can be seen from the figure, the theoretical predictions are able to provide an excellent qualitative description of the excess enthalpy at the pressures considered. Although the theory seems to over estimate the experimental values of the excess enthalpy, this could be due to the overestimation of the composition of the liquid–liquid boundaries at these conditions (see Fig. 5).

We have also considered the excess enthalpy of the mixture as a function of temperature. Fig. 9 shows the excess molar enthalpy of an equimolar gas mixture of $H_2O + H_2S$ at atmospheric pressure at different temperatures. As can be seen from the figure, the excess molar enthalpy decreases as we increase the temperature. The theory is able to capture this behavior although the agreement with the experimental data is only qualitative.

### 3.3. Henry's coefficients

Finally, we have considered the infinite-dilution mixture property the Henry's law constant of a solute in a solvent. McCabe et al. [39] have shown that the SAFT-VR approach can be used in a predictive way to study this property in aqueous mixtures and more recently, dos Ramos et al. [43] have been able to predict the Henry's coefficients of carbon dioxide in water using the same approach, where a qualitative agreement was achieved with both experimental and simulation data.

Fig. 10 shows the Henry's law constant at saturation pressure as a function of temperature for the binary system of hydrogen sulphide in water. The theory is able to describe the interesting behavior that this property exhibits: at low temperatures the value of the Henry's constants increases as we increase the temperature until the function reaches a maximum value ($H_{2,1}(P_1^{sat}, T) \approx 200$ MPa) at around 450K, and then decreases as the temperature is increased. It is interesting that the SAFT-VR+D approach is able to predict almost quantitatively the location of this maximum. However, the agreement between the theoretical predictions and the experimental data is only qualitative since at lower or higher temperatures the Henry's coefficient values are over predicted.

## 4. Conclusions

We have studied the thermodynamic properties of the water + hydrogen sulphide binary mixture using the SAFT-VR+D approach, where we have explicitly described the polar nature of both molecules. The molecular parameters used for water and hydrogen sulphide were taken from previous work [62,64] and used together with the standard Lorentz–Berthelot combining rules to determine the unlike interactions; the results are therefore obtained using only pure component parameters and as such are true predictions of the phase behavior.

The results show that the theory is able to predict the type *III* phase behavior observed experimentally with two separated critical lines and a three-phase liquid–liquid–vapor coexistence that runs from low temperatures up to the UCEP point. Additionally, a minimum in temperature in the high-pressure critical line is observed and suggests the possibility of gas–gas immiscibility of the second kind for which experimental measurements could be very difficult to perform. We also studied the phase equilibria over a range of high to low pressures and temperatures finding the agreement between experiments and theory very good in most cases.

We have also examined the excess molar enthalpy of the water + hydrogen sulphide binary mixture as a function of temperature and pressure. Considering that the excess functions are more sensitive to molecular details than phase equilibria, the good agreement achieved between the theoretical predictions and

experimental data, particularly at high-pressure conditions, is gratifying.

Finally, we have studied the Henry's constant of hydrogen sulphide in water as a function of temperature. The SAFT-VR+D approach was able to predict in a good qualitative manner the observed behavior of this property. In particular, the theory was able to locate the temperature at which there is a maximum in the Henry's law constant curve.

*List of symbols*

| | |
|---|---|
| $A$ | total Helmholtz free energy |
| $a^{M}$ | excess Helmholtz free energy per monomer |
| $a^{DSW}$ | excess Helmholtz free energy per monomer of the dipolar square-well reference fluid |
| $a^{isotropic}$ | excess Helmholtz free energy per monomer due to the isotropic interactions |
| $a^{dipole}$ | excess Helmholtz free energy per monomer due to the anisotropic dipolar interactions |
| $a^{HS}$ | excess Helmholtz free energy per monomer of the hard-sphere fluid |
| $a_1$ | first-order perturbation term |
| $a_2$ | second-order perturbation term |
| $[a_0]$ | $n \times n$ matrix defined in Eq. (22) |
| $[a_1]$ | $n \times n$ matrix defined in Eq. (24) |
| $[b_0]$ | $n \times n$ matrix defined in Eq. (23) |
| $[b_1]$ | $n \times n$ matrix defined in Eq. (25) |
| $\hat{c}_{ij}^{112}(r)$ | expansion coefficient of the direct correlation function |
| $f_{a,b,i,j}$ | Mayer $f$-function for the $a$–$b$ site-site interaction between sites on components $i$ and $j$ |
| $g_{ij}^{SW}$ | radial distribution function for the square-well fluid |
| $\hat{h}_{ij}^{112}(r)$ | expansion coefficient of the total correlation function |
| $H^{E}$ | excess molar enthalpy |
| $H^{E}_{x_1=0.5}$ | excess molar enthalpies at equimolar composition |
| $H_i$ | molar enthalpy of the pure fluid $i$ |
| $H_m$ | molar enthalpy of the mixture |
| $H_{2,1}(P_1^{sat}, T)$ | Henry's coefficient at saturation pressure of hydrogen sulphide in water |
| $\mathbf{I}$ | identity matrix of dimension $n \times n$ |
| $k_B$ | Boltzmann's constant ($1.3806503 \times 10^{-23}\,J\,K^{-1}$) |
| $k_{ij}$ | scaling parameters in the solution of the OZ equation |
| $[k]$ | scaling parameters matrix of dimension $n \times n$ |
| $K_{ii}^{HB}$ | site–site hydrogen bonding interaction volume between sites of component $i$ |
| $[K_0^0]$ | $n \times n$ matrix defined in Eq. (20) |
| $[K_1^0]$ | $n \times n$ matrix defined in Eq. (21) |
| $L_1$ | $H_2O$-rich liquid phase |
| $L_2$ | $H_2S$-rich liquid phase |
| $L_1$–$L_2$ | Liquid–liquid equilibria |
| $L_1$–V | $H_2O$-rich liquid–vapor equilibria |
| $L_2$–V | $H_2S$-rich liquid–vapor equilibria |
| $L_1$–$L_2$–V | liquid–liquid–vapor equilibria or LLVE |
| $N$ | total number of molecules |
| $n$ | number of components in the mixture |
| $N_s$ | total number of monomer segments |
| $\mathbf{n}_i$ | unit vector parallel to the dipole moment on segment $i$ |
| $P$ | pressure (MPa) |
| $[q_1]$ | $n \times n$ matrix defined in Eq. (16) |
| $[q_2]$ | $n \times n$ matrix defined in Eq. (17) |
| $r$ | distance between two dipolar spherical segments |
| $\mathbf{r}_{ij}$ | vector between the center of species $i$ and $j$ |
| $\hat{r}_{ij}$ | unit vector in the direction of $\mathbf{r}_{ij}$ |
| $r_c$ | cut-off radius for the hydrogen bonding attractive potential |
| $r_d$ | distance of the hydrogen bonding attractive site from the sphere center |
| $s_i$ | number of associating sites of the species $i$ |
| $T$ | temperature (K) |
| $u_{ij}$ | pair potential between component $i$ and $j$ |
| $u_{ij}^{HS}$ | hard-sphere repulsion pair potential between component $i$ and $j$ |
| $u_{ij}^{dipole}$ | dipole–dipole pair potential between component $i$ and $j$ |
| $u_{A_iB_j}^{HB}$ | association interaction pair potential between component $i$ and $j$ |
| $u_{int}^{dipole}$ | excess internal energy from the anisotropic dipolar contribution |
| $V$ | total volume of the system |
| $\mathbf{w}$ | set of angles that define the orientation of the dipole moment |
| $x_i$ | mole fraction of component $i$ |
| $X_{a,i}$ | fraction of molecules $i$ not bonded at site $a$ |
| $y_{ij}$ | strength of the dipolar effects of species $i$ interacting with species $j$ |
| $[y]$ | $n \times n$ matrix with elements $y_{ij}$ |
| $[z_t]$ | $n \times n$ matrix defined in Eq. (26) |

*Greek letters*

| | |
|---|---|
| $\beta$ | inverse of the temperature |
| $\delta_{ij}$ | delta Function |
| $\Delta_{a,b,i,j}$ | strength of the association between site $a$ on molecule $i$ and site $b$ on molecule $j$ |
| $\varepsilon$ | square-well potential depth parameter |
| $\varepsilon^{HB}$ | square-well potential depth parameter for the hydrogen bonding interaction |
| $\phi$ | polar angle of the dipole–dipole interaction |
| $\phi_{ij}^{SW}$ | shape of the square-well potential |
| $\phi_{a,b,i,j}$ | Shape of the $a$–$b$ site–site interaction square-well potential |
| $\lambda$ | square-well potential range parameter |
| $\Lambda_i$ | thermal de Broglie wavelength of species $i$ |
| $\mu$ | permanent dipole moment |
| $\theta$ | azimuthal angle of the dipole–dipole interaction |
| $\rho_i$ | number density of component $i$ |
| $[\rho^{1/2}]$ | $n \times n$ matrix whose elements are related to via Eq. (18) $\rho_i$ |
| $\sigma$ | hard-core segment diameter |
| $[\sigma]$ | $n \times n$ matrix whose elements are related to $\sigma$ via Eq. (19) |
| $\Omega_i$ | orientation of the association site $i$ relative to the vector $\mathbf{r}_{ij}$ |

*Superscripts*

| | |
|---|---|
| ASSOC | association |
| DSW | dipolar square-well |
| dipole | dipole |
| isotropic | isotropic |
| E | excess |
| HB | hydrogen bonding |
| MONO | monomer |
| M | monomer |
| sat | saturation |
| SW | square-well |
| $T$ | transpose of a matrix |
| * | parameters rescaled to the experimental critical point |

*Subscripts*

| | |
|---|---|
| $a,b$ | type of association sites |
| $A_i,B_j$ | interaction between associating sites on species $i$ and $j$ |
| $i,j$ | type of component |
| int | internal |
| m | mixture |
| UCEP | upper critical end point |

## Acknowledgments

We gratefully acknowledge financial support from the National Science Foundation under Grant No. CTS-0452688 and an REU supplement to CTS-0453641. We also thank Peter T. Cummings for useful discussions.

## References

[1] T.L. Guidotti, Occup. Med. 46 (1996) 367–371.
[2] J.M. Stellman (Ed.), Encyclopaedia of Occupational Health and Safety, vol. IV, 4th ed., International Labour Organization, Geneva, 1998.
[3] W.C. Lyons, G.J. Plisga (Eds.), Standard Handbook of Petroleum and Natural Gas Engineering, 2nd ed., Elsevier Inc., Oxford, 2005.
[4] D.S.J. Jones, P.P. Pujadú, Handbook of Petroleum Processing, 1st ed., Springer, Dordrecht, 2006.
[5] F. Al-Awadhy, I. Kocabas, J.H. Abou-Kassem, M.R. Islam, Energy Sources 27 (2005) 3–18.
[6] R.J. Reiffenstein, W.C. Hulbert, S.H. Roth, Annu. Rev. Pharmacol. Toxicol. 32 (1992) 109–134.
[7] D. Koschel, J.Y. Coxam, V. Majer, Ind. Eng. Chem. Res. 46 (2007) 1421–1430.
[8] J.A. Kent, Riegel's Handbook of Industrial Chemistry, 10th ed., Kluwer Academic/Plenum Publisher, New York, 2003.
[9] A. Chapoy, A.H. Mohammadi, B. Tohidi, A. Valtz, D. Richon, Ind. Eng. Chem. Res. 44 (2005) 7567–7574.
[10] F.T. Selleck, L.T. Carmichael, B.H. Sage, Ind. Eng. Chem. Res. 44 (1952) 2219–2226.
[11] T.N. Kozintseva, Geokhim. Issled. Obl. Povysh. Davlenii Temp. (1965) 121–134.
[12] M.P. Burgess, R.P. Germann, AlCHE J. 15 (1969) 272–275.
[13] E.C.W. Clarke, D.N. Glew, Can. J. Chem. 49 (1971) 691–698.
[14] K. Hiraoka, P. Kebarle, Can. J. Chem. 55 (1977) 24–28.
[15] J.I. Lee, A.E. Mather, Ber. Bunsen Ges. Phys. Chem. 81 (1977) 1020–1023.
[16] A.A. Douabul, J.P. Riley, Deep Sea Res. Part I 26 (1979) 259–268.
[17] P.C. Gillespie, G.M. Wilson, Vapor–Liquid Equilibrium Data on Water-Substitute Gas Components: $N_2$-$H_2O$, $H_2$-$H_2O$, CO-$H_2O$, $H_2$-CO-$H_2O$, and $H_2S$-$H_2O$, GPA Research Report, 1980.
[18] P.C. Gillespie, G.M. Wilson, Vapor–Liquid and Liquid–Liquid Equilibria: Water–Methane, Water–Carbon Dioxide, Water–Hydrogen Sulfide, Water–n-Pentane, Water–Methane–n-Pentane, GPA Research Report, 1982.
[19] T.J. Barrett, G.M. Anderson, J. Lugowski, Geochim. Cosmochim. Acta 52 (1988) 807–811.
[20] J.J. Carroll, A.E. Mather, Can. J. Chem. Eng. 67 (1989) 468–470.
[21] J.J. Carroll, A.E. Mather, Geochim. Cosmochim. Acta 53 (1989) 1163–1170.
[22] O.M. Suleimenov, R.E. Krupp, Geochim. Cosmochim. Acta 58 (1994) 2433–2444.
[23] B. Rumpf, A.P.S. Kamps, R. Sing, G. Maurer, Fluid Phase Equilib. 158 (1999) 923–932.
[24] C.J. Wormald, J. Chem. Thermodyn. 35 (2003) 1019–1030.
[25] J.J. Carroll, J. Can. Pet. Technol. 41 (2002) 39–43.
[26] H.H. Reamer, B.H. Sage, W.N. Lacey, Ind. Eng. Chem. Res. 43 (1951) 976–981.
[27] Z.H. Duan, R. Sun, R. Liu, C. Zhu, Energy Fuels 21 (2007) 2056–2065.
[28] G. Jackson, W.G. Chapman, K.E. Gubbins, Mol. Phys. 65 (1988) 1–31.
[29] W.G. Chapman, K.E. Gubbins, G. Jackson, M. Radosz, Ind. Eng. Chem. Res. 29 (1990) 1709–1721.
[30] M.S. Wertheim, J. Stat. Phys. 35 (1984) 19–34.
[31] M.S. Wertheim, J. Stat. Phys. 35 (1984) 35–47.
[32] M.S. Wertheim, J. Stat. Phys. 42 (1986) 459–476.
[33] M.S. Wertheim, J. Stat. Phys. 42 (1986) 477–492.
[34] E.A. Müller, K.E. Gubbins, Associating Fluids and Mixtures, in: J.V. Sengers, R.F. Kayser, C.J. Peters, H.J. White (Eds.), Equations of State for Fluids and Fluid Mixtures. Part 2, Elsevier Science, Amsterdam, 2000.
[35] E.A. Müller, K.E. Gubbins, Ind. Eng. Chem. Res. 40 (2001) 2193–2211.
[36] I.G. Economou, Ind. Eng. Chem. Res. 41 (2002) 953–962.
[37] G.N.I. Clark, A.J. Haslam, A. Galindo, G. Jackson, Mol. Phys. 104 (2006) 3561–3581.
[38] M.N.i. García-Lisbona, A. Galindo, G. Jackson, A.N. Burges, Mol. Phys. 93 (1998) 57–71.
[39] C. McCabe, A. Galindo, P.T. Cummings, J. Phys. Chem. B 107 (2003) 12307–12314.
[40] A. Galindo, A. Gil-Villegas, P.J. Whitehead, G. Jackson, A.N. Burgess, J. Phys. Chem. B 102 (1998) 7632–7639.
[41] A. Galindo, F.J. Blas, J. Phys. Chem. B 106 (2002) 4503–4515.
[42] F.J. Blas, A. Galindo, Fluid Phase Equilib. 194–197 (2002) 501–509.
[43] M.C. dos Ramos, F.J. Blas, A. Galindo, J. Phys. Chem. C 111 (2007) 15924–15934.
[44] M.C. dos Ramos, F.J. Blas, A. Galindo, Fluid Phase Equilib. 261 (2007) 359–365.
[45] T. Kraska, K.E. Gubbins, Ind. Eng. Chem. Res. 35 (1996) 4738–4746.
[46] T. Kraska, K.E. Gubbins, Ind. Eng. Chem. Res. 35 (1996) 4727–4737.
[47] E.A. Müller, K.E. Gubbins, Ind. Eng. Chem. Res. 34 (1995) 3662–3673.
[48] K. Xu, Y.G. Li, W.B. Liu, Fluid Phase Equilib. 142 (1998) 55–66.
[49] P.K. Jog, W.G. Chapman, Mol. Phys. 97 (1999) 307–319.
[50] P.K. Jog, S.G. Sauer, J. Blaesing, W.G. Chapman, Ind. Eng. Chem. Res. 40 (2001) 4641–4648.
[51] J. Gross, J. Vrabec, AICHE J. 52 (2006) 1194–1204.
[52] M. Kleiner, J. Gross, AICHE J. 52 (2006) 1951–1961.
[53] E.K. Karakatsani, I.G. Economou, J. Phys. Chem. B 110 (2006) 9252–9261.
[54] E.K. Karakatsani, T. Spyriouni, I.G. Economou, AICHE J. 51 (2005) 2328–2342.
[55] K.E. Gubbins, C.G. Gray, Mol. Phys. 23 (1972) 187–191.
[56] G. Stell, J.C. Rasaiah, H. Narang, Mol. Phys. 23 (1972) 393–406.
[57] F. Tumakaka, G. Sadowski, Fluid Phase Equilib. 217 (2004) 233–239.
[58] B. Larsen, J.C. Rasaiah, G. Stell, Mol. Phys. 33 (1977) 987–1027.
[59] E.K. Karakatsani, G.M. Kontogeorgis, I.G. Economou, Ind. Eng. Chem. Res. 45 (2006) 6063–6074.
[60] E.K. Karakatsani, I.G. Economou, Fluid Phase Equilib. 261 (2007) 265–271.
[61] H. Zhao, C. McCabe, J. Chem. Phys. 125 (2006) 104504.
[62] H. Zhao, Y. Ding, C. McCabe, J. Chem. Phys. 127 (2007) 084514.
[63] M.S. Wertheim, J. Chem. Phys. 55 (1971) 4291–4298.
[64] M.C. dos Ramos, K.D. Goff, H.G. Zhao, C. McCabe, J. Phys. Chem. B 112 (2008) 9417–9427.
[65] S.A. Adelman, J.M. Deutch, J. Chem. Phys. 59 (1973) 3971–3980.
[66] P.T. Cummings, L. Blum, J. Chem. Phys. 84 (1986) 1833–1842.
[67] P.T. Cummings, L. Blum, J. Chem. Phys. 85 (1986) 6658–6667.
[68] F.J. Blas, Mol. Phys. 100 (2002) 2221–2240.
[69] F.J. Blas, J. Phys. Chem. B 104 (2000) 9239–9248.
[70] F.J. Blas, I. Fujihara, Mol. Phys. 100 (2002) 2823–2838.
[71] W. Bol, Mol. Phys. 45 (1982) 605–616.
[72] I. Nezbeda, J.v.i. Kolafa, Y.V. Kalyuzhnyi, Mol. Phys. 68 (1989) 143–160.
[73] T.R. Forester, I.R. McDonald, M.L. Klein, Chem. Phys. 129 (1989) 225–234.
[74] T. Kristof, J. Liszi, J. Phys. Chem. B 101 (1997) 5480–5483.
[75] C.G. Gray, K.E. Gubbins, Theory of Molecular Fluids: Fundamentals International Series of Monographs on Chemistry 9, vol. I, Oxford University Press, New York, USA, 1985.
[76] A. Gil-Villegas, A. Galindo, P.J. Whitehead, S.J. Mills, G. Jackson, A.N. Burgess, J. Chem. Phys. 106 (1997) 4168–4185.
[77] A. Galindo, L.A. Davies, A. Gil-Villegas, G. Jackson, Mol. Phys. 93 (1998) 241–252.
[78] J.P. Hansen, I.R. McDonald, Theory of Simple Liquids, 2nd ed., Elsevier Academic Press, London, 1990.
[79] J.A. Barker, D.J. Henderson, J. Chem. Phys. 47 (1967) 2856–2861.
[80] J.A. Barker, D.J. Henderson, J. Chem. Phys. 47 (1967) 4714–4721.
[81] J.A. Barker, D.J. Henderson, Rev. Mod. Phys. 48 (1976) 587–671.
[82] T.J. Boublík, J. Chem. Phys. 53 (1970) 471–472.
[83] G.A. Mansoori, N.F. Carnahan, K.E. Starling, T.W. Leland, J. Chem. Phys. 54 (1971) 1523–1525.
[84] D. Isbister, B.C. Freasier, R.J. Bearman, Aust. J. Chem. 33 (1980) 1953–1966.
[85] L. Sun, H. Zhao, S.B. Kiselev, C. McCabe, J. Phys. Chem. B 109 (2005) 9047–9058.
[86] R.L. Scott, P.H. van Konynenburg, Faraday Discuss. 49 (1970) 87–97.
[87] P.H. van Konynenburg, R.L. Scott, Philos. Trans. R. Soc. London Ser. A A298 (1980) 495–540.
[88] C. McCabe, S.B. Kiselev, Ind. Eng. Chem. Res. 43 (2004) 2839–2851.
[89] L.X. Sun, H.G. Zhao, S.B. Kiselev, C. McCabe, J. Phys. Chem. B 109 (2005) 9047–9058.
[90] C. McCabe, S.B. Kiselev, Fluid Phase Equilib. 219 (2004) 3–9.
[91] L.X. Sun, H.G. Zhao, S.B. Kiselev, C. McCabe, Fluid Phase Equilib. 228 (2005) 275–282.
[92] J.S. Rowlinson, F.L. Swinton, Liquids and Liquid Mixtures, 3rd ed., Butterworth Scientific, London, 1982.
[93] D.R. Lide (Ed.), CRC Handbook of Chemistry and Physics, 88th ed., CRC Press/Taylor and Francis, Boca Raton, FL, 2007.
[94] R.J. Gulley, M.J. Brunger, S.J. Buckman, J. Phys. B: At. Mol. Opt. Phys. 26 (1993) 2913–2925.
[95] B.H. Sage, W.N. Lacey, Some Properties of the Lighter Hydrocarbons, Hydrogen Sulfide, and Carbon Dioxide, American Petroleum Institute, New York, 1955.
[96] C.F. Beaton, G.F. Hewitt, Physical Property Data for the Design Engineer, Hemisphere Publishing Corp., New York, 1989.